Geophysical Journal International

Geophys. J. Int. (2017) **210,** 1806–1822
Advance Access publication 2017 June 20
GJI Seismology

doi: 10.1093/gji/ggx269

High-frequency seismic wave propagation within the heterogeneous crust: effects of seismic scattering and intrinsic attenuation on ground motion modelling

Shunsuke Takemura,[1] Manabu Kobayashi[2] and Kazuo Yoshimoto[2]

[1]*National Research Institute for Earth Science and Disaster Resilience,* 3-1 *Tennodai, Tsukuba, Ibaraki* 305-0006*, Japan. E-mail: shunsuke@bosai.go.jp*
[2]*Department of Material System Science, Graduate School of Nanobioscience, Yokohama City University,* 22-2 *Seto, Kanazawa-ku, Yokohama* 236-0027*, Japan*

Accepted 2017 June 19. Received 2017 June 14; in original form 2017 January 12

SUMMARY

For practical modelling of high-frequency (>1 Hz) seismic wave propagation, we analysed the apparent radiation patterns and attenuations of *P* and *S* waves using observed Hi-net velocity seismograms for small-to-moderate crustal earthquakes in the Chugoku region, southwestern Japan. By comparing observed and simulated seismograms, we estimated practical parameter sets of crustal small-scale velocity heterogeneity and intrinsic attenuations of *P* and *S* waves ($Q_{P.\mathrm{int}}{}^{-1}$ and $Q_{S.\mathrm{int}}{}^{-1}$). Numerical simulations of seismic wave propagation were conducted via the finite-difference method using a 1-D crustal velocity structure model with additional 3-D small-scale velocity heterogeneity and intrinsic attenuation. The estimated crustal small-scale velocity heterogeneity is stochastically characterized by an exponential-type power spectral density function with correlation length of 1 km and root-mean-square value of 0.03. Estimated $Q_{P.\mathrm{int}}{}^{-1}$ and $Q_{S.\mathrm{int}}{}^{-1}$ values range from $10^{-2.6}$ to $10^{-2.0}$ and $10^{-2.8}$ to $10^{-2.4}$, respectively, indicating $Q_{P.\mathrm{int}}{}^{-1} > Q_{S.\mathrm{int}}{}^{-1}$ for high frequencies (>1 Hz). Intrinsic attenuation dominates over scattering attenuation, which is caused by small-scale velocity heterogeneity. The crustal parameters obtained in this study are useful for evaluating peak ground velocities and coda envelopes for moderate crustal earthquakes via physical-based simulations using a 3-D heterogeneous structure model.

Key words: Body waves; Coda waves; Earthquake ground motions; Seismic attenuation; Wave propagation; Wave scattering and diffraction.

1 INTRODUCTION

In order to achieve ground motion prediction for hazardous earthquakes, attenuations of peak ground acceleration and velocity (PGA and PGV) as a function of hypocentral distance have been studied in various regions of the world (e.g. Boore & Joyner 1982; Si & Midorikawa 1999; Baltay & Beroza 2013; Yabe *et al*. 2014). Estimated empirical attenuation curves well explain the average characteristics of observed ground motions, and have been widely used in applications such as source energy estimation, ground motion evaluation, and earthquake early warning (e.g. Boatwright 2007; Kamigaichi *et al*. 2009; Yabe & Ide 2014; Bostock *et al*. 2015; Furumura 2016; Takemura *et al*. 2016). Although the empirical attenuation curves bring information on the quality factors of *P*- and *S*-wave apparent attenuations (Q_P and Q_S; e.g. Boatwright *et al*. 1991; Yoshimoto *et al*. 1993; Yabe *et al*. 2014), information on intrinsic and scattering attenuations, which are required for physics-based ground motion predictions via 3-D simulation, cannot be directly deduced from these curves. In order to estimate intrinsic and scattering attenuation separately, multiple-lapse time window analysis (MLTWA) has been conducted in the world (e.g. Fehler *et al*. 1992; Jin *et al*. 1994; Padhy *et al*. 2007; Carcolé & Sato 2010). These studies, in which very simplified structure models (e.g. infinite homogeneous media with uniformly distributed scatterers) were commonly assumed, reported that the dominant mechanism of attenuation of *S* waves is intrinsic attenuation for frequencies greater than 1 Hz (summarized in fig. 8.13 of Sato *et al*. 2012).

Many studies have reported that the spatial distribution of observed maximum *S*-wave amplitudes during local earthquakes (hereafter called the 'apparent *S*-wave radiation pattern') is gradually distorted from the expected four-lobe amplitude pattern of a double-couple point source with increasing frequency and distance (e.g. Liu & Helmberger 1985; Satoh 2002; Takenaka *et al*. 2003; Takemura *et al*. 2009). Combined analysis of observations and simulations using heterogeneous velocity models have pointed out that the frequency- and distance-dependent characteristics of the apparent *S*-wave radiation pattern can be explained as a result of seismic wave scattering due to small-scale

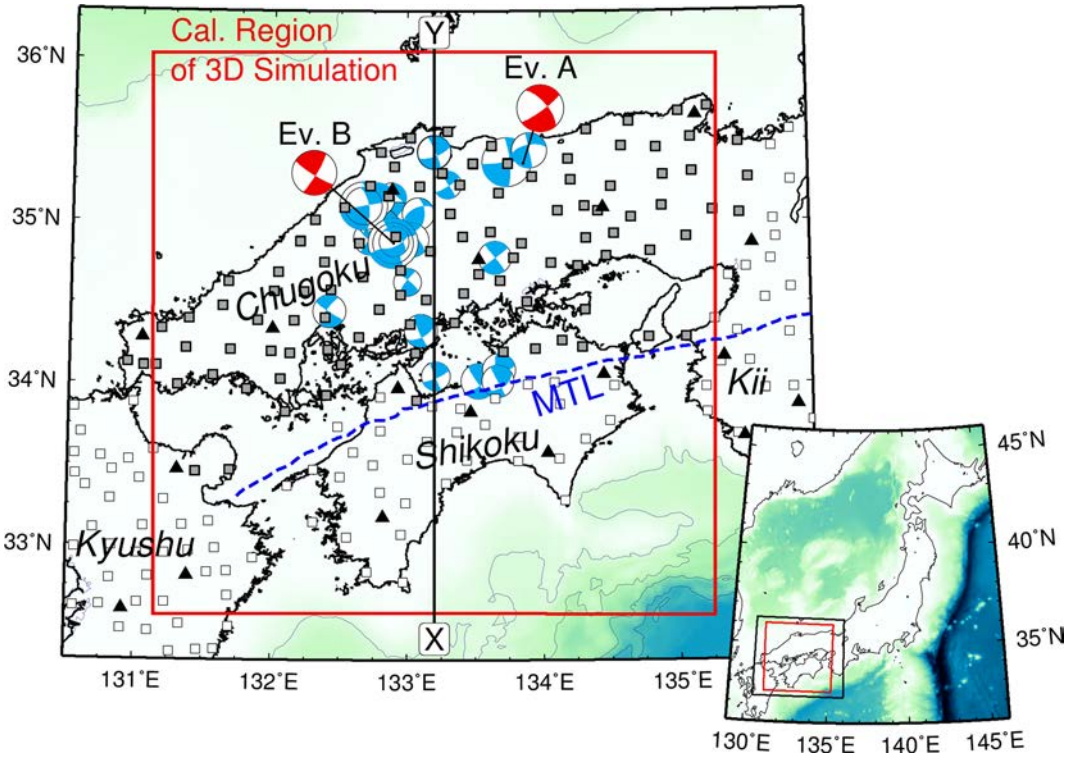

Figure 1. Distribution of seismic stations and epicentres used in this study. Squares and triangles denote Hi-net and F-net stations, respectively. Grey filled squares are stations used in parameter estimations in this study. Parameters of each source are listed in Table 1 and Supporting Information Table S1. Earthquakes with blue and red focal spheres are used in parameter estimations and validations, respectively. Red rectangle represents horizontal coverage of calculation region of 3-D FDM simulations using 3-D heterogeneous layered structure model. Assumed velocity structure model along line X–Y in later large-scale simulations is shown in Fig. 10(a). Blue dashed line is Median Tectonic Line (MTL) of Japan.

velocity heterogeneity in the crust (e.g. Takemura *et al*. 2009, 2015a; Kumagai *et al*. 2011; Imperatori & Mai 2013, 2015; Morioka *et al*. 2016). Theoretical studies of envelope synthetics incorporating the frequency- and distance-dependent apparent radiation pattern have also been developed. For example, Sawazaki *et al*. (2011) applied their Markov approximation technique for synthesizing three-component vector wave envelopes to explain the observed characteristics of azimuthal variations in seismogram envelopes.

Dense seismic networks enable us to investigate the detailed characteristics of frequency- and distance-dependent apparent radiation patterns of not only *S* waves but also *P* waves. Applying the coda-normalization method to borehole records of crustal earthquakes, Kobayashi *et al*. (2015) found that the apparent *P*-wave radiation pattern is also gradually distorted with increasing frequency and distance. Using the same method for *P* and *S* wave analysis, Takemura *et al*. (2016) demonstrated that distortion of the apparent radiation patterns could be simply characterized by a function of the normalized distance (the product of frequency and distance), irrespective of wave type. Despite these studies, it is still difficult to evaluate the frequency- and distance-dependent characteristics of strong ground motions (e.g. PGV). To achieve this, practical models of crustal small-scale velocity heterogeneity and intrinsic attenuation are required.

In this study, to estimate crustal parameters for small-scale velocity heterogeneity and intrinsic attenuation for modelling high-frequency *P*- and *S*-wave propagations, we analyse seismograms of local crustal earthquakes and synthetic seismograms via 3-D finite-difference-method (FDM) simulations of seismic wave propagation in heterogeneous crust models. By comparing observed and simulated seismograms, we estimate practical parameter sets for crustal small-scale velocity heterogeneity and intrinsic attenuation. We also conduct 3-D FDM simulations of moderate crustal earthquakes and demonstrate that our model practically reproduces the observed PGVs, shapes of coda envelopes, and characteristics of seismic record sections.

2 DATA AND METHOD

2.1 Observed data

Our target region is the Chugoku region, southwestern Japan (Fig. 1), where strike-faulting earthquakes occur in the crust (e.g. Terakawa & Matsu'ura 2010). We analyse velocity seismograms recorded at high-sensitivity seismograph network (Hi-net; Okada *et al*. 2004; Obara *et al*. 2005) operated by the National Research Institute for Earth Science and Disaster Resilience, Japan (NIED), during 31 strike-faulting crustal earthquakes. The frequency response of the short-period Hi-net sensors is corrected using the program of Maeda *et al*. (2011). Hypocentre locations and focal mechanisms are referred from the Hi-net hypocentre catalogue (details are shown in Supporting Information Table S1 and

Fig. S1). Blue focal spheres in Fig. 1 are estimated using first-motion polarizations recorded at Hi-net stations. We select 104 Hi-net stations that are within hypocentral distances of 150 km, and are located north of the median tectonic line (MTL), which is a major geological and seismic attenuation boundary (e.g. Liu & Zhao 2015) in southwestern Japan. The total numbers of seismograms are 2074 (*P* for 0.5–1 Hz), 2042 (*S* for 0.5–1 Hz), 2077 (*P* for 1–2 Hz), 2057 (*S* for 1–2 Hz), 2071 (*P* for 2–4 Hz), and 2061 (*S* for 2–4 Hz).

In order to eliminate the differences in site amplification and source size, we employ the coda-normalization technique (e.g. Aki 1980; Yoshimoto *et al*. 1993). A uniform spatial distribution of *S*-coda amplitudes in the epicentre region at large lapse times was demonstrated by the radiative transfer theory for a shear dislocation source (Sato *et al*. 1997). Coda-normalized maximum *P*- and *S*-wave amplitudes (hereafter, '*P*-wave amplitude' and '*S*-wave amplitude', respectively) are measured from the root-mean-square vector envelopes (hereafter, simply called 'RMS envelope') of the three-component (NS, EW and UD) seismograms for three frequency bands: 0.5–1 Hz, 1–2 Hz, and 2–4 Hz. The central frequencies (f_c) of each band are 0.75, 1.5 and 3 Hz, respectively. The time windows of τ-seconds, which are average pulse durations of *P*- and *S*-wave displacement waveforms at the four nearest broad-band seismometers (filled triangles in Fig. 1) of the NIED full-range seismograph network (F-net; Okada *et al*. 2004), are used to measure maximum *P*- and *S*-wave amplitudes. We employ lapse times of 60–70 s for calculating averaged coda amplitudes used in the coda normalization procedure. Examples of coda-normalized RMS envelopes and *P*- and *S*-wave amplitudes are shown in Supporting Information Fig. S2.

2.2 Finite-difference method simulation of seismic wave propagation

Seismic wave propagations through heterogeneous crust models are evaluated via FDM simulations solving equations of motion in 3-D elastic or viscoelastic media. The 3-D simulation model covers an area of 200 × 200 × 120 km^3, which is discretized by a uniform grid interval of 0.1 km. In order to conduct 3-D simulations effectively, we employ a parallel FDM simulation code based on a domain partitioning procedure using large number processors, employing the Message Passing Interface (after Furumura & Chen 2004). Other technical details are described in Takemura *et al*. (2015a). We adopt the 1-D crustal velocity structure model of Ukawa *et al*. (1984) for the background velocity structure in our simulations. We do not assume low-velocity sedimentary layers in the model. According to the minimum *S*-wave velocity of this model (3.25 km s^{-1}) and assumed grid interval, our simulations can be used to examine seismic wave propagation for frequencies up to $f = 4.0$ Hz (wavelength $\lambda = 0.8$ km) with a sampling of eight grid points per minimum *S* wavelength. Simulations are conducted using the computer system at the Earthquake and Volcano Information Centre, Earthquake Research Institute, the University of Tokyo. Each simulation requires 624.2 GB of computer memory and a wall-clock time of 2.3 hr by parallel computing using 384 cores of the system to evaluate seismic wave propagation of 50 s with 10 000 time-step calculations.

A double-couple point source of pure strike-slip faulting ($M_{xy} = 1.0$) with an asymmetric cosine source-time function (Ji *et al*. 2003) with $t_s = t_e = 0.25$ s and $M_o = 1.26 \times 10^{15}$ Nm (M_w 4.0) is set at the centre of the model at 10 km depth. Radiated seismic waves are observed at dense virtual seismic stations that are uniformly distributed on the free surface at an interval of 2.5 km (6400 stations). Maximum *P*- and *S*-wave amplitudes are measured using a 0.5-s window from the onset times because of the 0.5-s pulse duration of the source time function.

In order to model small-scale velocity heterogeneities in the crust, we employ stochastic random velocity fluctuations characterized by a von Kármán-type power spectral density function (PSDF) in the wavenumber domain (Klimeš 2002; Sato *et al*. 2012):

$$P(k) = \frac{8\pi^{3/2}\Gamma(\kappa + 3/2)\varepsilon^2 a^3}{\Gamma(\kappa)(1 + a^2k^2)^{\kappa+3/2}}, \quad (1)$$

where ε is the RMS value of the fluctuation, a is the correlation length, k is the wavenumber, and κ is the decay rate parameter of the PSDF at larger k. In the case of $\kappa = 0.5$, the von Kármán PSDF coincides with the exponential-type PSDF. The spatial seismic velocity fluctuation, $\xi(\boldsymbol{x})$, is embedded over the 1-D crust model as $V_0(\boldsymbol{x})$ as $V(\boldsymbol{x}) = V_0(\boldsymbol{x})[1 + \xi(\boldsymbol{x})]$. We assume correlated velocities (V_P and V_S) and density ρ from Birch's law (Birch 1961; Sato *et al*. 2012).

In order to estimate the practical parameter set for the small-scale velocity heterogeneity model for the crust, we compare frequency- and distance-dependent characteristics of simulated apparent radiation patterns with observed ones. We employ the parameters $a = 1$–3 km, $\varepsilon = 0.03$–0.05, and $\kappa = 0.5$ based on previous studies (e.g. Takemura *et al*. 2009, 2015a; Kobayashi *et al*. 2015; Yoshimoto *et al*. 2015) and no small-scale velocity heterogeneity in the mantle (e.g. Margerin *et al*. 1999). In our previous study (Kobayashi *et al*. 2015), we tested frequency- and distance-dependent characteristics of the apparent *P*-wave radiation pattern using FDM simulations of 12 different stochastic velocity fluctuation models. An exponential-type small-scale velocity heterogeneity with $a = 1$ km and $\varepsilon = 0.03$ practically reproduced the observed characteristics of the apparent *P*-wave radiation pattern. Thus, we conduct FDM simulations of this model and three additional models to obtain a parameter set of crustal small-scale velocity heterogeneity. In the strict sense, the trade-off problem in the estimation of a and ε (e.g. Gaebler *et al*. 2015) might be considered more carefully for the analysis of broad-band seismic data. However, we treat this point as a topic for future study and restrict the target frequency of our data analysis to 0.5–4 Hz.

We conduct FDM simulations using three realizations of random velocity fluctuations for the same parameter set to evaluate the statistical properties of the simulated wavefields. The symmetry of the radiation pattern of the pure strike-slip faulting source enables us to obtain 12 quadrant results of azimuthal changes in *P*- and *S*-wave amplitudes. To introduce frequency-dependent intrinsic attenuation ($Q_{\mathrm{Int}}{}^{-1}$; Robertsson *et al*. 1994) of *P* and *S* waves, we adopt a single relaxation mechanism model, which can be controlled by two parameters: the reference frequency f_0 and peak value $Q_0{}^{-1}$. Technical details about $Q_{\mathrm{int}}{}^{-1}$ in the FDM simulations are described in Maeda *et al*. (2013).

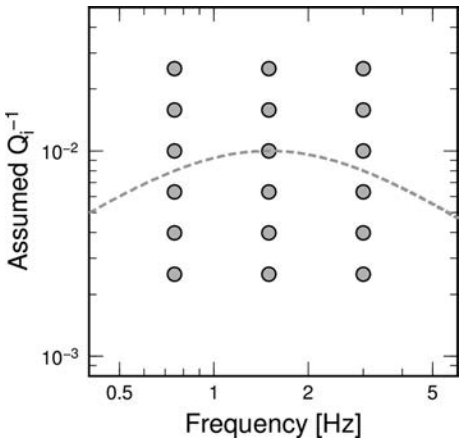

Figure 2. Frequency-dependent $Q_{\text{int}}{}^{-1}$ models for *P* and *S* waves based on a single relaxation mechanism (Robertsson *et al.* 1994). Each grey circle denotes initially assumed peak values of $Q_0{}^{-1}$. Reference frequency f_0 is the same as the central frequencies of each band (f_c = 0.75, 1.5 and 3 Hz). Dashed line represents frequency-dependent feature of a single-relaxation Zener body with $Q_0{}^{-1} = 1.0 \times 10^{-2}$ and f_0 = 1.5 Hz.

The frequency-dependent feature of this description is confirmed in Fig. 2 (dashed line). The values of $Q_0{}^{-1}$ are almost constant around the reference frequency, f_0.

2.3 Method for estimating parameters of crustal heterogeneity and attenuation

2.3.1 Parameters of crustal small-scale velocity heterogeneity

We analyse the frequency- and distance-dependent characteristics of the apparent radiation patterns for *P* and *S* waves. Based on the method by Kobayashi *et al.* (2015), we calculate the 'observed (or simulated) amplitude fluctuation $\delta A_j(k,L_i,\phi_i)$' using the following equation:

$$\delta A_j\,(k, L_i, \phi_i) = \frac{A_j\,(k, L_i, \phi_i) - A_{0j}\,(k, L_i)}{A_{0j}\,(k, L_i)}\,(j = P, S)\,, \tag{2}$$

where $A_j(k, L_i)$ is the *P*- or *S*-wave amplitude for wavenumber k ($=2\,\pi/\lambda = 2\pi f_c/V_j$) at a hypocentral distance of L_i, ϕ_i is the azimuth from the fault strike at the *i*th station and $A_{0j}(k,L_i)$ is the attenuation curve (solid lines in Supporting Information Fig. S2b). V_j is the seismic velocity of *P* or *S* waves in the crust (assumed to be 6.00 and 3.55 km s^{-1}, respectively). The azimuthal difference in amplitude fluctuations reflects the apparent radiation pattern (see fig. 2 of Takemura *et al.* 2016). Attenuation curves of the *P* and *S* waves $A_{0j}(k, L_i)$ are estimated using the following equation:

$$\ln\left(L_i A_j\,(k, L_i, \phi_i)\right) = r L_i + C, \tag{3}$$

where r and C are constant values. Since the hypocentral distance, L_i, is commonly used as an independent parameter for attenuation analysis in engineering seismology (e.g. Si & Midorikawa 1999; Baltay & Beroza 2013), we simply assume $1/L_i$ as geometrical spreading of body waves, rather than the inverse of the exact ray path length. Supporting Information Fig. S2b shows the observed *P*- and *S*-wave amplitudes and attenuation curves for frequencies of 0.5–1 and 2–4 Hz as examples.

We also calculate theoretical amplitude fluctuations, defined as the fluctuation of the theoretical radiation pattern coefficient, $|F_j|$, from its azimuthal average at a hypocentral distance of L_i. Theoretical radiation pattern coefficients are evaluated assuming a double-couple point source (Aki & Richards 2002, Ch. 4) within the 1-D velocity structure model (Ukawa *et al.* 1984). Then, we calculate the cross-correlation coefficient (CCC) between observed and theoretical amplitude fluctuations:

$$\mathrm{CCC}\,(k, L) = \frac{\sum_{i=1}^{N}\left[\delta A_{\text{amp}}\,(k, L_i, \phi_i) - \overline{\delta A_{\text{amp}}\,(k, L)}\right]\left[\delta A_{\text{theo}}\,(k, L_i, \phi_i) - \overline{\delta A_{\text{theo}}\,(k, L)}\right]}{\sqrt{\sum_{i=1}^{N}\left[\delta A_{\text{amp}}\,(k, L_i, \phi_i) - \overline{\delta A_{\text{amp}}\,(k, L)}\right]^2}\sqrt{\sum_{i=1}^{N}\left[\delta A_{\text{theo}}\,(k, L_i, \phi_i) - \overline{\delta A_{\text{theo}}\,(k, L)}\right]^2}}. \tag{4}$$

Here, δA_{amp} and δA_{theo} are the observed (or simulated) and theoretical amplitude fluctuations. L is the central hypocentral distance of a certain distance window (40–70, 50–80, 60–90, 70–100, 80–110, 90–120 and 100–130 km). The resulting CCC quantitatively reflects the distortion of the apparent radiation pattern; the four-lobe pattern is identified as CCC = 1, and isotropic pattern as CCC = 0. Since the major cause of the distortion of the apparent radiation pattern with increasing frequency and distance is seismic wave scattering due to small-scale velocity heterogeneity (e.g. Takemura *et al.* 2015a), we compare observed and simulated CCCs for various frequency bands and hypocentral

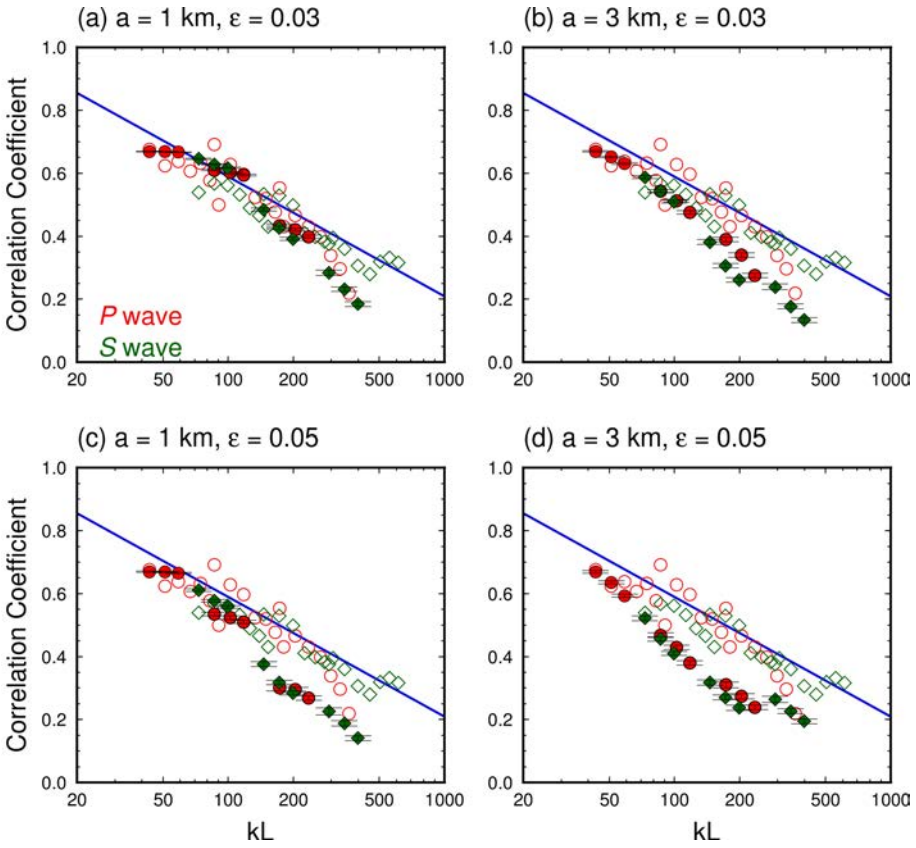

Figure 3. Normalized hypocentral distance (kL) dependence in CCCs for observed/simulated and theoretical fluctuations. Estimation error of CCC was evaluated using the bootstrap method (Efron & Tibshirani 1986). Averaged CCC and estimation error were calculated for 100 sets of random resampling data. Open circles and diamonds are observed CCCs for P and S waves, respectively. Blue line denotes kL-CCC relationship from our previous observation study (Takemura *et al.* 2016), which is characterized by the function CCC $\propto -0.38 \log(kL)$. Filled symbols are the same as open ones, but for simulation results, which are shifted to be consistent with the observed CCC at the nearest kL (= 43.2). The levels of shifts of simulated CCCs in (a)–(d) are 0.29, 0.25, 0.23 and 0.14, respectively.

distances (Fig. 3) to estimate parameter set of small-scale velocity heterogeneity within the crust. The estimated model can explain the frequency- and distance-dependent properties of the observed CCCs for both P and S waves. After the estimation, model parameters for small-scale velocity heterogeneity will be fixed in later simulations for attenuation analysis.

2.3.2 Apparent attenuation and intrinsic attenuation

We estimate the apparent attenuation Q^{-1} for observed P and S waves in the crust using the following equation:

$$\ln\left(L_i A_j\left(L_i\right)\right) = -\frac{\pi f_c Q_{j.\mathrm{app.}}^{-1}}{V_j} L_i + C'\,(j = P, S) \tag{5}$$

where ${Q_{\mathrm{j,app.}}}^{-1}$ is the quality factor for the apparent P- or S-wave attenuations and C' is a constant. We note that the apparent attenuation, ${Q_{\mathrm{j,app.}}}^{-1}$, includes both intrinsic and scattering attenuations. Generally, the data in the nodal directions of the source radiation pattern would cause inaccurate estimation of the attenuation characteristics. In this analysis, to discard amplitude data in the nodal directions and to obtain attenuation characteristics within the crust, we select data $A_{\mathrm{j}}(L_{\mathrm{i}})$ with distances of 30–90 km and $|F_{\mathrm{j}}|$ values equal to or greater than 0.63, which is the average radiation pattern coefficient for S wave (Boore & Boatwright 1984).

Since the scattering attenuation is uniquely characterized by the small-scale velocity heterogeneity, which could be estimated by the analysis of CCC, on the basis of a grid-search inversion technique, we can estimate intrinsic attenuation of P and S wave for minimizing the normalized residual between observed and simulated apparent attenuations:

$$\mathrm{residual} = \frac{\left|{Q_{\mathrm{app.obs}}}^{-1} - {Q_{\mathrm{app.simu}}}^{-1}\right|}{{Q_{\mathrm{app.obs}}}^{-1}}, \tag{6}$$

where ${Q_{\mathrm{app.obs}}}^{-1}$ and ${Q_{\mathrm{app.simu}}}^{-1}$ are observed and simulated apparent attenuations, respectively.

Fig. 2 shows ${Q_0}^{-1}$ values used in the grid-search parameter estimation: ${Q_0}^{-1} = 10^{-2.6}$, $10^{-2.4}$, $10^{-2.2}$, $10^{-2.0}$, $10^{-1.8}$ and $10^{-1.6}$. We set the reference frequency, $f_{0,}$ to be equal to the central frequency of each frequency band; consequently, the ${Q_{\mathrm{int}}}^{-1}$ value is almost constant

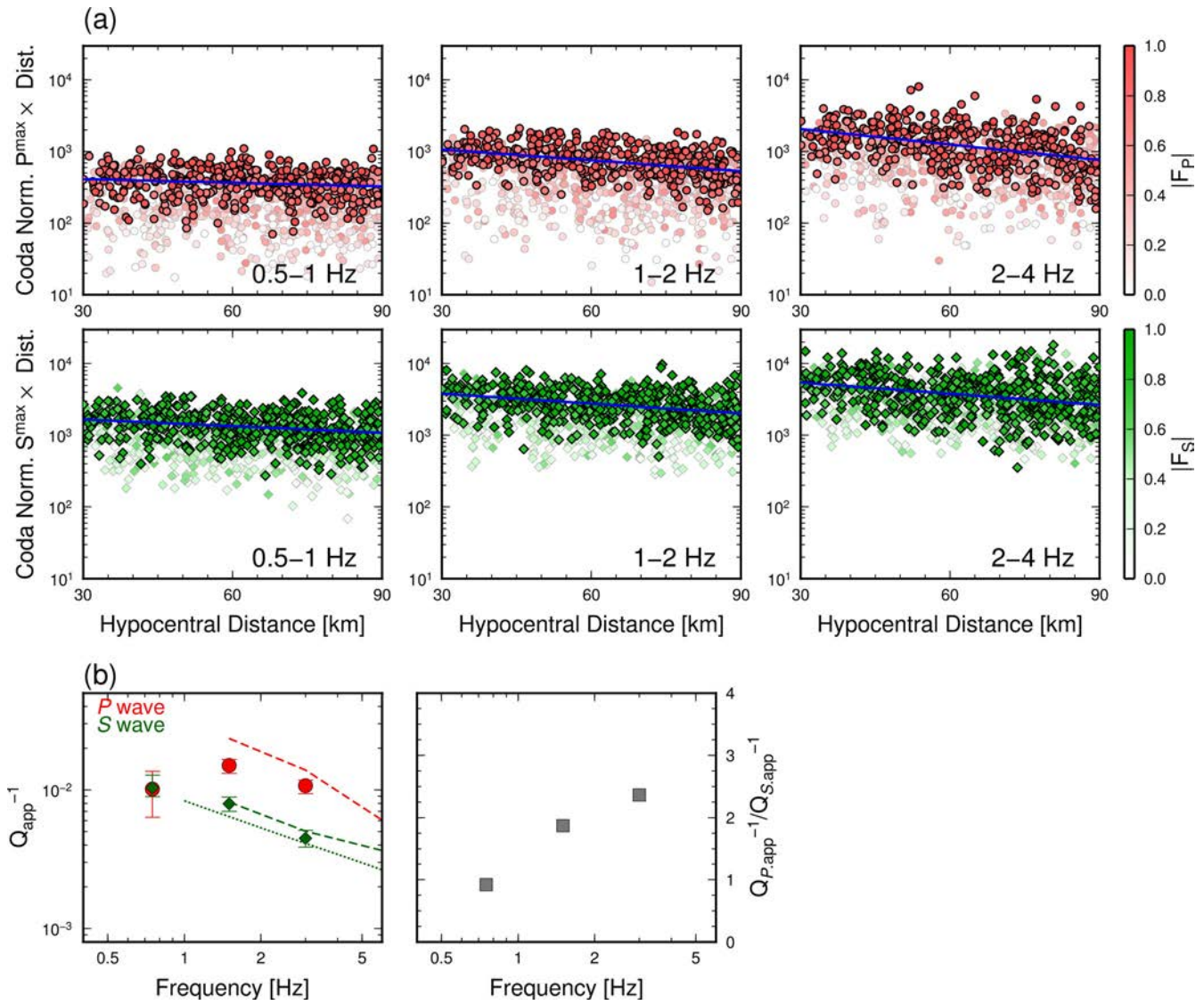

Figure 4. (a) Distance change in observed coda-normalized maximum *P*- and *S*-wave amplitudes (P^{max} and S^{max}) and (b) estimated observed apparent attenuation for frequencies of 0.5–1, 1–2 and 2–4 Hz. In order to enhance data at far stations, each amplitude is multiplied by its hypocentral distance. Red circles and green diamonds denote coda-normalized amplitudes for *P* and *S* waves, respectively. Enhanced symbols indicate data with $|F_j|$ equal to or greater than 0.63, which are used in estimation of apparent attenuations. Blue lines are attenuation master curves derived from selected data using eq. (4). Red and green dashed lines in (b) are apparent attenuations for *P* and *S* waves from Yoshimoto *et al*. (1993). Green dotted line is apparent *S* wave attention estimated by Zhang *et al*. (2016).

($= Q_0^{-1}$) within each frequency band (see grey dashed line in Fig. 2). We regard the Q_0^{-1} value giving the smallest normalized residual as the Q_{int}^{-1} value of the crust, and the Q_0^{-1} range where the normalized residual becomes smaller than the estimation error of observed apparent attenuation as the estimation error.

3 RESULTS

3.1 Observed characteristics of the apparent *P*- and *S*-wave radiation patterns

Fig. 3 shows CCCs between observed and theoretical amplitude fluctuations as a function of normalized hypocentral distance *kL*. The observed CCCs in this study (open symbols) are in good agreement with our previous study in the same region (blue line in Fig. 3; Takemura *et al*. 2016), which was obtained via regression analysis of CCCs from 13 crustal earthquakes. CCCs decay linearly with increasing log(*kL*), irrespective of wave type. The CCCs in this study can be described by CCC $\propto -0.37 \log(kL)$, which corresponds well to our previous work (CCC $\propto -0.38 \log(kL)$). Simulated CCCs are evaluated for hypocentral distances of 40–70, 50–80 and 60–90 km because of the limitation of our simulation settings.

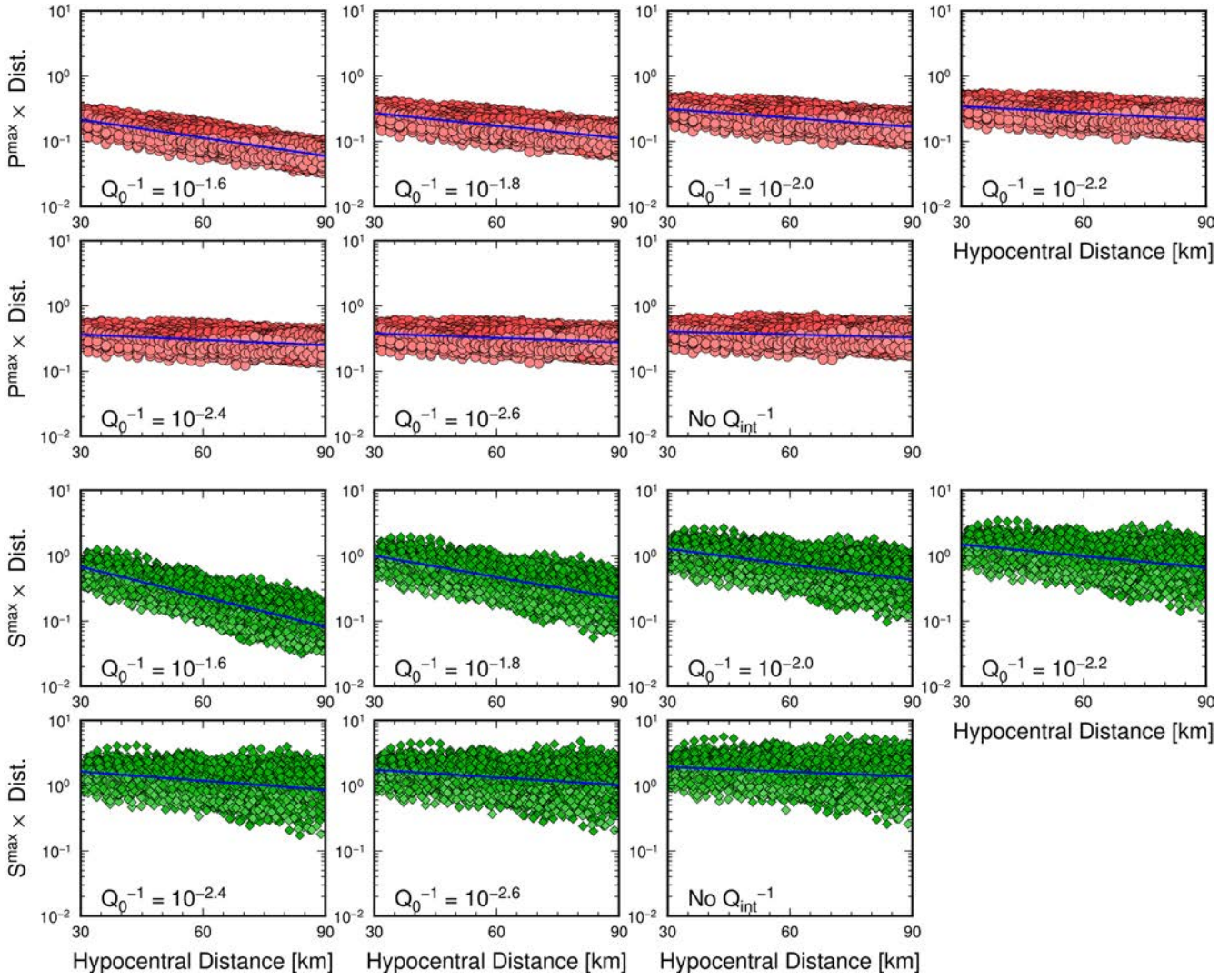

Figure 5. Simulated maximum amplitudes of *P* and *S* waves (P^{max} and S^{max}) for frequencies of 1–2 Hz. In order to enhance data at far stations, each amplitude is multiplied by its hypocentral distance. Red circles and green diamonds denote amplitudes for *P* and *S* wave, respectively. Amplitudes are measured at 30–90 km stations with $|F_j|$ equal to or greater than 0.63. Reference frequency of Zener body is 1.5 Hz, and assumed ${Q_0}^{-1}$ values are shown in lower-left corner of each subfigure. Blue lines are attenuation master curves derived from selected data using eq. (4).

In order to evaluate optimal parameters for small-scale velocity heterogeneity within the crust, we also plotted simulated CCCs derived from four different heterogeneous models (filled symbols). We shifted the absolute levels of simulated CCCs to be consistent with the observed CCCs at the nearest kL (= 43.2) to eliminate possible non-modelling effects, such as complex source rupture and localized heterogeneities around source faults, and to compare their decay rate for normalized hypocentral distances.

The simulation result with $a = 1$ km and $\varepsilon = 0.03$ (Fig. 3a) successfully reproduces the observed kL-dependence features of CCCs, while the CCCs of other models decay more rapidly. Based on comparing the kL-CCC relationship between observation and simulations, we confirm that distortion of the apparent *P*- and *S*-wave radiation patterns with increasing frequency and distance is caused by seismic wave scattering due to crustal small-scale heterogeneity characterized by an exponential-type PSDF with $a = 1$ km and $\varepsilon = 0.03$. It is worthy of note that this model also successfully explains the variance of the observed *P*-wave amplitude levels for crustal earthquakes in the same region (Yoshimoto *et al*. 2015).

3.2 Attenuation of *P* and *S* waves

Fig. 4(a) shows observed *P*- and *S*-wave amplitudes with $|F_j|$ values equal to or greater than 0.63 (enhanced symbols) as a function of hypocentral distance. The fluctuations of the amplitudes decrease compared to those of the all data. Blue lines are attenuation curves derived from the data using eq. (4). Estimated apparent attenuation ${Q_{j.app}}^{-1}$ values (Fig. 4b) are consistent with other studies in Japan (e.g. Yoshimoto *et al*. 1993; Zhang *et al*. 2016). The ratios ${Q_{P.app}}^{-1}/{Q_{S.app}}^{-1}$ have the same range as those reported in previous studies (summarized in fig. 5.13 of Sato *et al*. 2012).

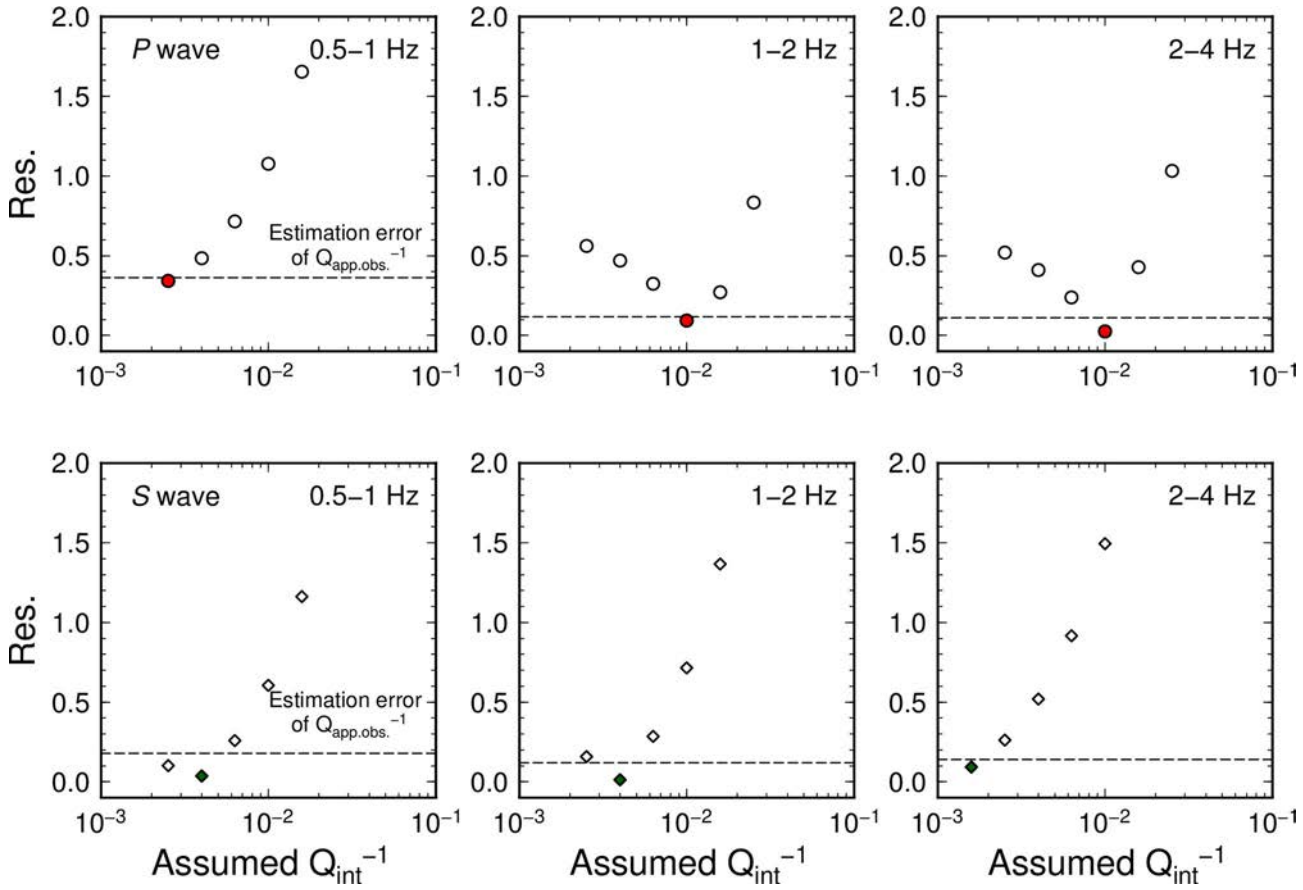

Figure 6. Normalized residual between observed and simulated apparent attenuations as a function of assumed Q_0^{-1} value. Circles and diamonds denote normalized residual for *P* and *S* waves, respectively. Filled symbols denote best-fit parameters for each frequency band.

Assuming a small-scale velocity heterogeneity model ($a = 1$ km and $\varepsilon = 0.03$) obtained from the analysis of CCC, we evaluate the intrinsic attenuations in the crust by comparing the observed and simulated apparent attenuations of the *P* and *S* waves. For example, Fig. 5 shows simulated *P*- and *S*-wave amplitudes for frequencies of 1–2 Hz assuming various Q_0^{-1} values and $f_0 = 1.5$ Hz. Simulation results without Q_{int}^{-1}, reflecting only the effects of scattering attenuation, show much weaker distance attenuation rates compared to observations (Fig. 4). This result indicates that intrinsic attenuation is a dominant attenuation mechanism in the crust, except for highly heterogeneous regions such as subduction zones and volcanic regions (Takahashi *et al*. 2009; Takahashi 2012; Takemura & Yoshimoto 2014; Takemura *et al*. 2015b).

As the Q_0^{-1} value increases, the decay of the amplitudes against hypocentral distance becomes stronger. Based on the analysis of normalized residuals (eq. 6), we estimate the optimal Q_0^{-1} values, or Q_{int}^{-1} values of the crust, for three frequency bands: 0.5–1, 1–2 and 2–4 Hz (Fig. 6). We successfully find the Q_{int}^{-1} value (filled symbols in Fig. 6), which lets the normalized residual be small compared to the estimation error of observed apparent attenuations, for all frequency bands. The estimation error for Q_{int}^{-1} is expected to be one or half of a grid interval of our grid search inversion, except for *P* waves of 0.5–1 Hz and *S* wave of 2–4 Hz. Fig. 7(a) shows estimated Q_{int}^{-1} values for *P* and *S* waves as a function of frequency.

4 DISCUSSION AND APPLICATIONS

4.1 Validation of our assumptions

In estimating the small-scale velocity heterogeneity, our simulations did not include the effects of intrinsic attenuation. After estimating the small-scale velocity heterogeneity, intrinsic attenuations were estimated via FDM simulations under the assumption that $Q_{P.int}^{-1} = Q_{S.int}^{-1}$. In this subsection, we validate these two assumptions via additional FDM simulations. Because of the insensitiveness of our validation tests to frequency, we show the results for frequencies of 1–2 Hz as examples.

Fig. 8 shows comparisons of simulation results between models with/without intrinsic attenuation. In the simulation using the model with intrinsic attenuation, we employ a single relaxation Zener body with a reference frequency of $f_0 = 1.5$ Hz, $Q_{P0}^{-1} = 10^{-2.0}$, and $Q_{S0}^{-1} = 10^{-2.4}$ (Fig. 7a), which are the optimal parameter set for frequencies of 1–2 Hz. Spatial patterns of maximum *P*- and *S*-wave amplitudes are not changed by introducing intrinsic attenuations, while amplitudes decrease because of intrinsic attenuation. These features are also found in

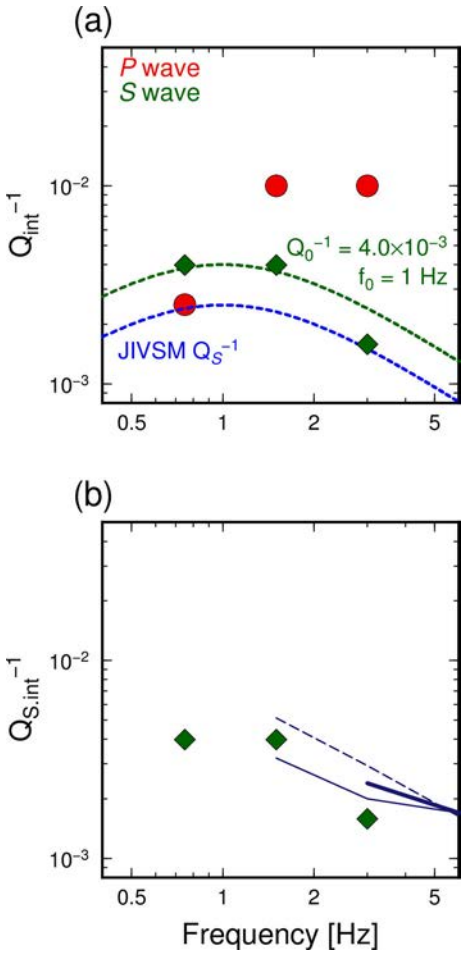

Figure 7. (a) Estimated intrinsic attenuations for *P* and *S* waves as a function of frequency. Green dashed line represents Zener body with $Q_0{}^{-1} = 4.0 \times 10^{-3}$, $f_0 = 1$ Hz, which are used in 3-D FDM simulations for moderate crustal earthquakes. A Zener body for *S* waves referred from JIVSM (Koketsu *et al*. 2012) is also plotted as blue dashed line. (b) Comparative plot of intrinsic *S* attenuations between this and previous studies. Solid, dashed and bold lines in (b) are intrinsic *S* attenuations estimated by Hoshiba (1993), Carcolé & Sato (2010) and Sawazaki *et al*. (2011), respectively.

RMS envelopes derived from the same simulations (Fig. 8c). Amplitude ratios between node and anti-node directions are almost the same, irrespective of the variation in intrinsic attenuation. This implies that intrinsic attenuation does not contribute much to the frequency- and distance-dependent characteristics of distortion of the apparent radiation patterns.

We here check the effect of the assumption that $Q_{P.\mathrm{int}}{}^{-1} = Q_{S.\mathrm{int}}{}^{-1}$ in estimating intrinsic attenuations. Fig. 9 shows the spatial variation of maximum amplitudes (Fig. 9a,b) and amplitude ratios (Fig. 9c) for models with the same $Q_{\mathrm{int}}{}^{-1}$ and different $Q_{\mathrm{int}}{}^{-1}$ for *P* and *S* waves. In the spatial variations of maximum amplitudes and ratios, discrepancies can be seen only in the nodal directions of *P* and *S* waves, with very small magnitudes. In our analysis, we used data with $|F_j|$ values equal to or greater than 0.63, which are not located in the nodal directions. Thus, we may conclude that the assumption that $Q_{P.\mathrm{int}}{}^{-1} = Q_{S.\mathrm{int}}{}^{-1}$ has no significant influence on the estimations of intrinsic attenuations.

4.2 Attenuation structure in Chugoku region, southwestern Japan

Our analysis indicates that the dominant mechanism of attenuations in the crust is intrinsic attenuation, and the $Q_{P.\mathrm{int}}{}^{-1}$ and $Q_{S.\mathrm{int}}{}^{-1}$ values range from $10^{-2.6}$ to $10^{-2.0}$ and $10^{-2.8}$ to $10^{-2.4}$, respectively. We here compare our estimation of apparent attenuations with those of previous studies around Chugoku region, Japan. Our estimated intrinsic attenuations for frequencies of 2–4 Hz roughly correspond to the total Q^{-1} values estimated by attenuation tomography (e.g. Liu & Zhao 2015; Kita & Matsubara 2016) and analysis of tectonic tremors (Yabe *et al*. 2014). Hoshiba (1993), Carcolé & Sato (2010) and Sawazaki *et al*. (2011) separately estimated intrinsic and scattering *S*-wave attenuations using synthetic envelopes based on radiative transfer or Markov approximation theories. Fig. 7(b) shows a comparative plot of intrinsic attenuations from this and previous studies as a function of frequency. Our estimations of intrinsic *S*-wave attenuations roughly correspond to the other results.

We employed a depth-varying background velocity structure model with the Moho discontinuity in the FDM simulations. Furthermore, to focus our attention on *P* and *S* waves restricted to the crust, we carefully employed τ-sec (<1 s) time windows for measuring maximum amplitudes. By employing these methods for observed waveforms of crustal earthquakes, we estimated intrinsic attenuations, $Q_{P.\mathrm{int}}{}^{-1}$ and

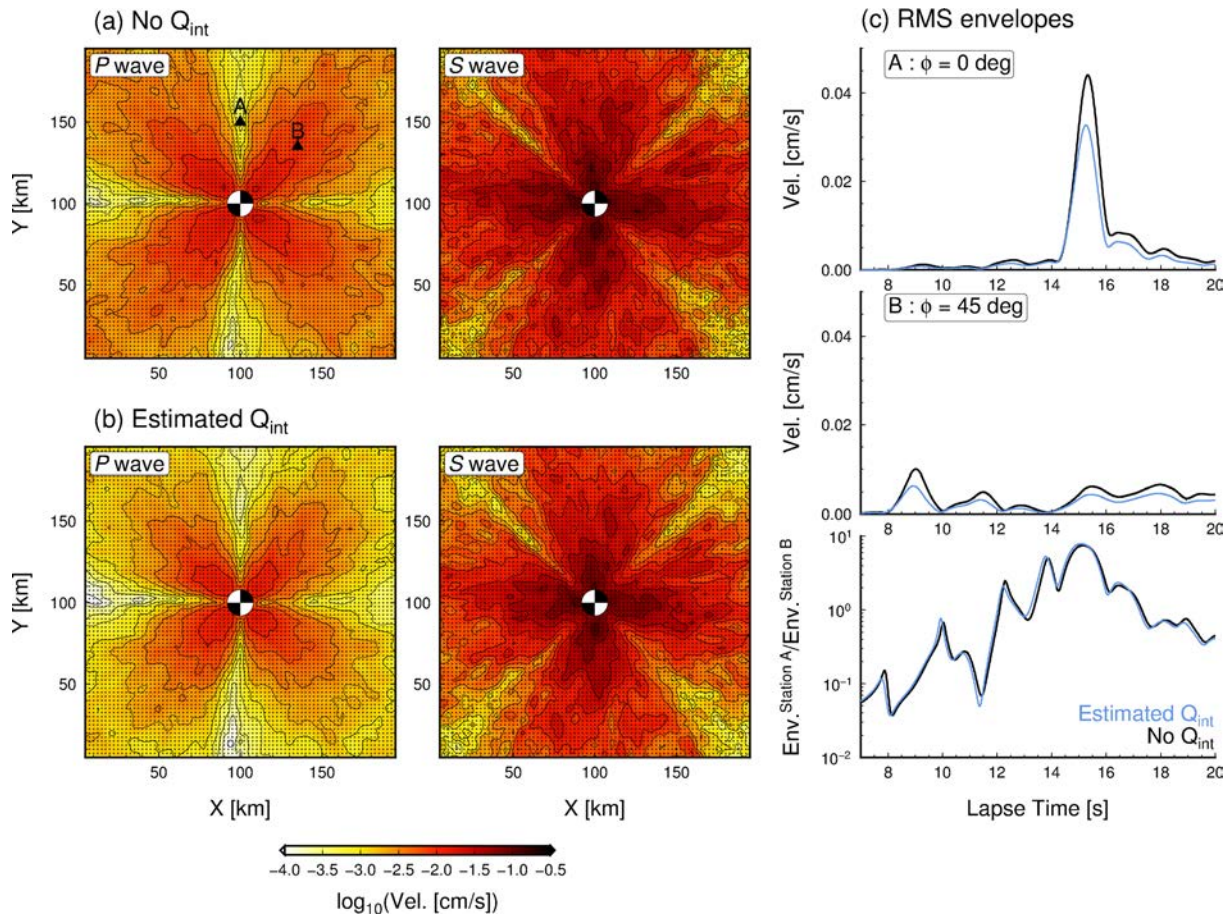

Figure 8. Comparison between simulation results with/without $Q_{\rm int}$. Spatial variations of *P*- and *S*-wave amplitudes for frequencies of 1–2 Hz derived from simulation results (a) without $Q_{\rm int}$ and (b) with optimal $Q_{\rm int}$ model. (c) Comparison of simulated RMS envelopes. Stations used in (c) are plotted in left subfigure of (a). Bottom subfigure in (c) is amplitude ratio between envelopes at stations A and B.

$Q_{S.\rm int}{}^{-1}$, specific not to the lithosphere but to the crust. Our simulation revealed the relationship $Q_{P.\rm int}{}^{-1} > Q_{S.\rm int}{}^{-1}$ for high (>1 Hz) frequencies. This finding, and the observed inequality $Q_{\rm int}{}^{-1} > Q_{\rm scat}{}^{-1}$, (Figs 4 and 5) imply that the physical mechanism of the well-known observational relationship $Q_{P.\rm app}{}^{-1} > Q_{S.\rm app}{}^{-1}$ (fig. 5.13 of Sato *et al*. 2012) should be explained as being caused by seismic absorption rather than scattering.

4.3 Strong ground motion simulations for crustal earthquakes

To confirm that our estimated parameters are also useful for evaluation of ground motions for moderate crustal earthquakes, we conduct additional FDM simulations for Event A ($M_{\rm w}$ 4.7) and Event B ($M_{\rm w}$ 4.4), which were not used in our parameter estimations. To compare the simulation results with observations of not only PGVs but also coda envelopes, the simulation model covers a larger zone (384 × 384 × 128 km^3; red square in Fig. 1) compared to previous simulations. The grid intervals and technical details are the same as in previous simulations. The large-scale FDM simulations are effectively conducted using 128 (512 cores) nodes of the Earth Simulator on the Japan Agency for Marine-Earth Science and Technology. Each simulation requires a wall-clock time of 2.5 hr to evaluate seismic wave propagation for 120 s.

The 3-D layered background velocity structure is obtained from the Japan Integrated Velocity Structure Model (JIVSM; Koketsu *et al*. 2012), including the surface topography, Conrad, Moho, and subducting Philippine Sea plate. Although various velocity structure models were proposed, the crustal structure of JIVSM, which would affect the reproducibility of traveltimes and low-frequency seismograms, is consistent with other models (e.g. Shiomi *et al*. 2006; Matsubara *et al*. 2017). Fig. 10(a) shows a cross-section of the assumed background velocity structure along the X–Y profile. We note that JIVSM $Q_S{}^{-1}$ values have been used for wider frequency ranges (0.016–2 Hz) in previous studies (e.g. Maeda *et al*. 2013; Takemura & Yoshimoto 2014; Takemura *et al*. 2015b,c; Kubo *et al*. 2016) and for evaluating long-period ground motion hazard maps for Japan (http://www.jishin.go.jp/evaluation/seismic_hazard_map/lpshm/12_choshuki/).

We employ F-net moment tensor (MT) solutions (Fukuyama *et al*. 1998; Kubo *et al*. 2002) for two crustal earthquakes (Events A and B) to model double-couple point sources. We adopt a source time function represented by an asymmetric cosine function (Ji *et al*. 2003). Durations of source time functions, which are based on the relationship between seismic moment and rupture duration (Kanamori & Brodsky 2004; Archuleta & Ji 2016), and other parameters for Events A and B are listed in Table 1. Fourier spectra of observed Hi-net velocity waveforms and time-series of assumed source time functions for each event are shown in Figs 10(b) and (c), respectively. Using displacement

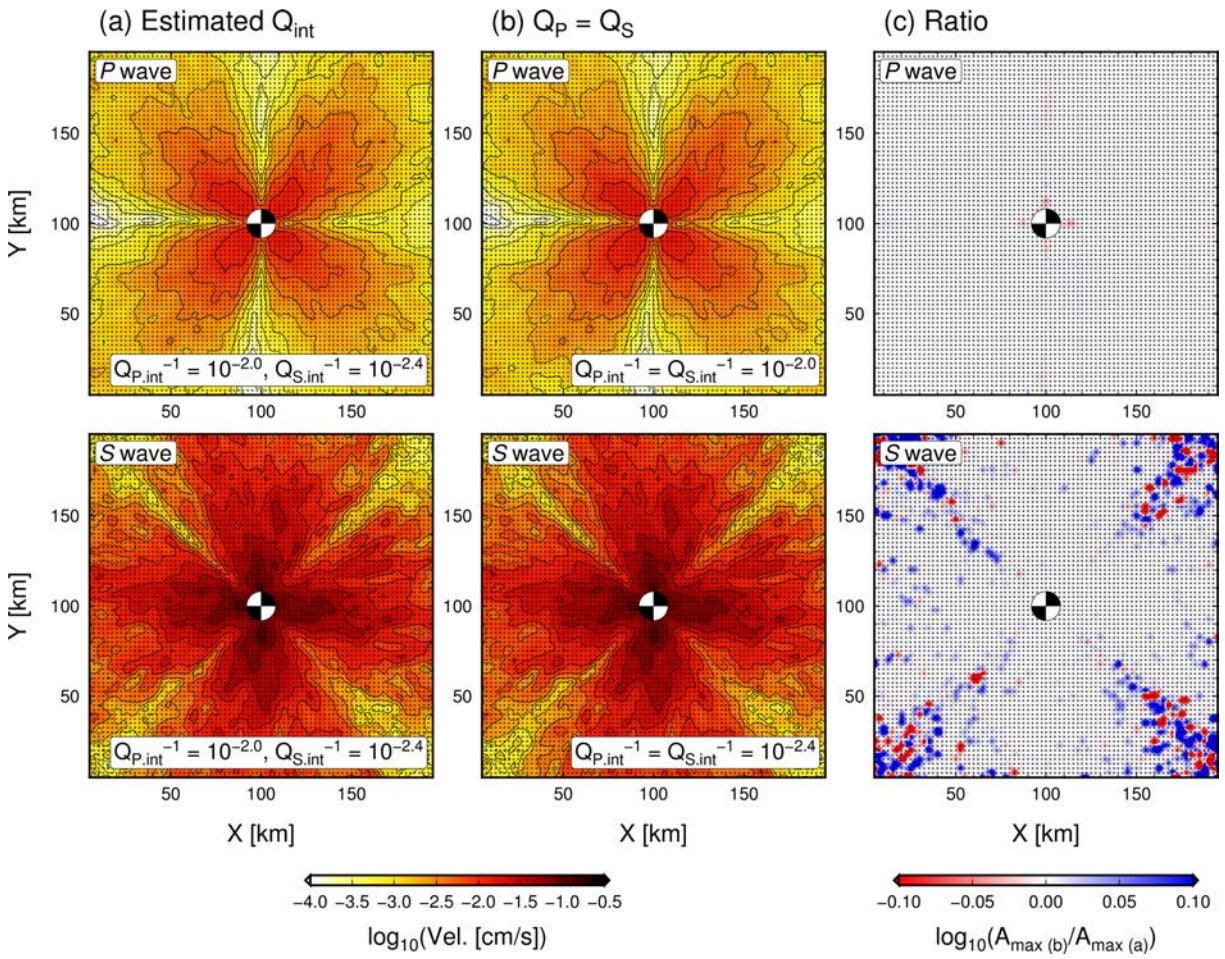

Figure 9. Comparison of simulation results using different and the same Q_{int}^{-1} models for *P* and *S* waves. Spatial variation of maximum *P*- and *S*-wave amplitudes for frequencies of 1–2 Hz derived from (a) optimal Q_{int}^{-1} model ($Q_{P.int}^{-1} = 10^{-2}$, $Q_{S.int}^{-1} = 10^{-2.4}$) and (b) optimal models for *P* wave ($Q_{P.int}^{-1} = Q_{S.int}^{-1} = 10^{-2}$) and *S* wave ($Q_{P.int}^{-1} = Q_{S.int}^{-1} = 10^{-2.4}$). (c) Spatial distribution of amplitude ratios between model (a) and model (b) *P* and *S* waves. Wave types and parameters assumed in simulation are shown in upper-left and lower-right corners of subfigures (a) and (b).

waveforms observed at the nearest F-net stations, the seismic moments *M*o for Events A and B are adjusted to 76 per cent and 88 per cent, respectively, to adjust the difference between the JIVSM and F-net 1-D structure (Kubo *et al*. 2002) models.

The small-scale heterogeneity estimated in the previous sections is embedded in the crust of the JIVSM. We employ a single relaxation Zener body with $Q_{S0}^{-1} = Q_{P0}^{-1} = 4.0 \times 10^{-3}$ and $f_0 = 1$ Hz (green dashed line in Fig. 7a) in the crust. Since estimated intrinsic attenuations have a complex frequency dependence (Fig. 7a) that could not be easily modelled by a simple Zener body, we focus our attention on the reproducibility of the PGVs and *S*-coda waves of the target earthquakes. Later coda waves are mainly constructed with *S* and surface waves for frequencies of 0.5–4 Hz (e.g. Sato *et al*. 2012, Ch. 3). Other Q_0^{-1} values beneath the crust are obtained from the original JIVSM. In order to obtain the ensemble averaged RMS envelopes, we conduct FDM simulations with 10 realizations of the constructed 3-D model, including small-scale velocity heterogeneity. PGV values are measured from the averaged RMS envelopes.

In our simulations, we do not assume a shallow low-velocity ($V_S < 3$ km s^{-1}) sedimentary and seawater layer; consequently, our FDM simulation can evaluate seismic wave propagation for frequencies up to 4 Hz. The effects of low-velocity sediments for Hi-net borehole records would be expected to be very weak compared to K-NET/KiK-net surface strong motion records. We compare observed and simulated PGVs of Hi-net horizontal seismograms for frequencies of 0.1–4 Hz.

Fig. 11 shows spatial variations and distance attenuations of PGVs derived from observed and simulated velocity waveforms. We also conduct FDM simulations using the original JIVSM (model 1) as a reference, where original Q_S^{-1} values (blue lines in Fig. 7a) and no small-scale velocity heterogeneity are assumed. Observed and simulated PGVs appear in *S* waves at distance less than 150 km, but at distances greater than 150 km in *Lg* waves (see Supporting Information Fig. S3), which are constructed by multiple reflections of *S* waves between the free surface and the Moho (e.g. Furumura *et al*. 2003, 2014). Empirical attenuation functions of surface PGV proposed by Si & Midorikawa (1999), which were derived from surface strong ground motion records and are widely used for evaluating strong ground motions (e.g. Furumura 2016) and earthquake early warnings (e.g. Kamigaichi *et al*. 2009) in Japan, are also plotted. Since Hi-net stations are located

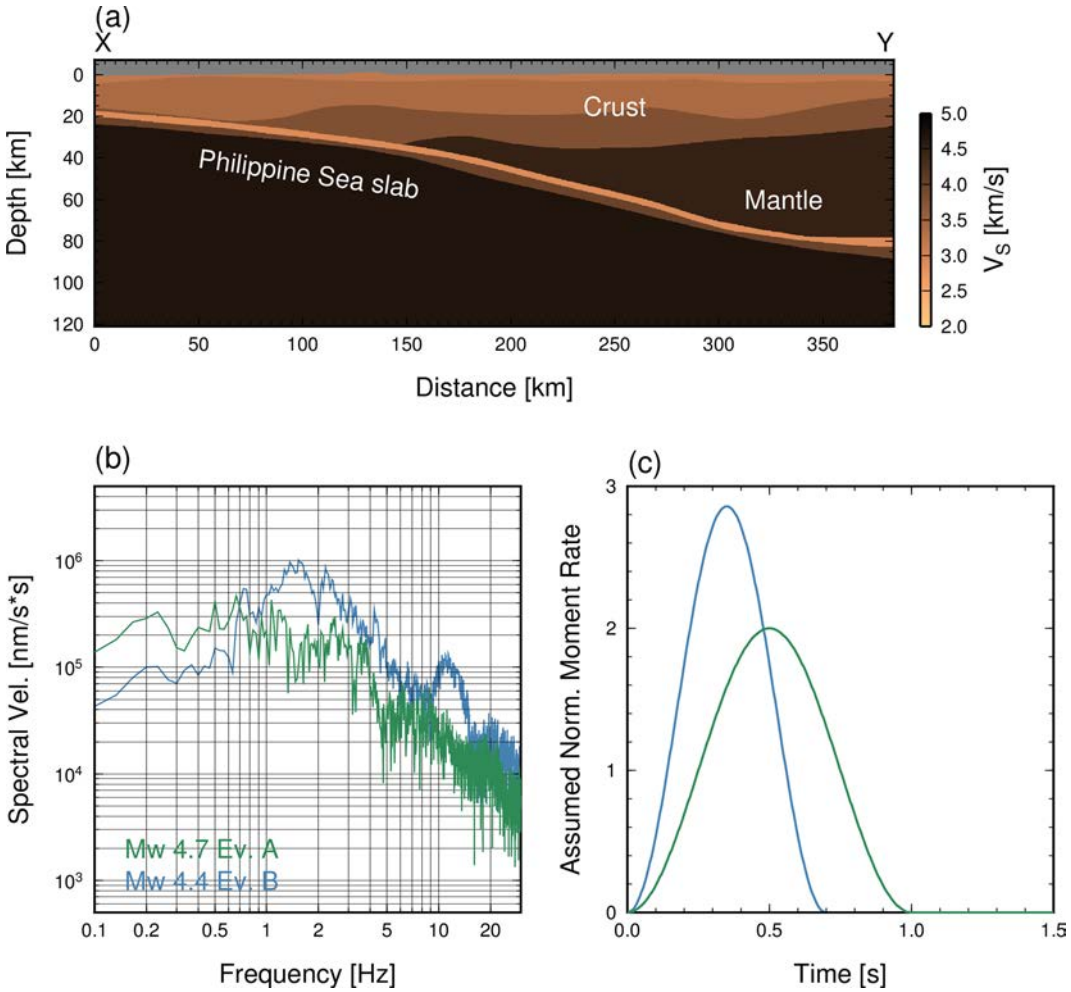

Figure 10. (a) Cross-section of JIVSM *S*-wave structure along X–Y profile in Fig. 1, (b) observed velocity spectrum of Hi-net waveforms, and (c) assumed moment rate functions for events A and B. Each spectral amplitude is calculated using horizontal waveforms at each nearest Hi-net station.

Table 1. Earthquakes considered in this study. Origin time, hypocentre, focal mechanism, moment magnitude and duration of source time function for Events A and B are listed.

#	DATE (JST)	Latitude (°N)	Longitude (°E)	Depth (km)	Strike (°)	Dip (°)	Rake (°)	M_w	Duration (s)
A	2016/10/21, 14:53:17	133.87	35.36	5	320	67	−10	4.7	1.0
B	2011/11/25, 04:35:26	132.89	34.87	14	122	83	8	4.4	0.7

at depths of several hundred meter, to compensate for the difference between surface and borehole ground motions, empirical attenuation functions are divided by a factor of two.

Since dominant frequencies for Events A and B are approximately 1 and 1.5 Hz (see Figs 10b–c), respectively, spatial distributions of both observed and simulated PGVs still preserve the clear four-lobe patterns expected from F-net MT solutions. However, the characteristics of distance attenuations of the PGVs are different between the two models. Simulation results of model 1 (original JIVSM; middle panels of Fig. 11) for both earthquakes are overestimated at distances of 50–300 km. Although simulation of model 2 for Event A is still overestimated compared to the observations, discrepancies between the observations and simulations can be reduced by introducing small-scale velocity heterogeneity and optimal intrinsic attenuation models (model 2; right panels of Fig. 11).

We also compare logarithmic plots of observed and simulated RMS envelopes to confirm the reproducibility of the seismic wavefield, including the later coda portion. Fig. 12 shows comparisons of observed and simulated RMS envelopes. Simulations of model 2 (red lines) do well in reproducing not only the maximum amplitudes but also the later coda amplitudes. In the simulation results of model 1 (green lines), propagations of *S* and *Lg* waves are consistent with the observations (Supporting Information Fig. S3), but the amplitudes are overestimated and the coda waves do not decay smoothly with increasing lapse time. Recent numerical studies, including surface topography (e.g. Hartzell *et al*. 2014, 2017; Imperatori & Mai 2015; Takemura *et al*. 2015a), demonstrated that coda waves are strongly excited by scattering due to surface topography alone, but were not able to reproduce the observed smooth and long-duration codas.

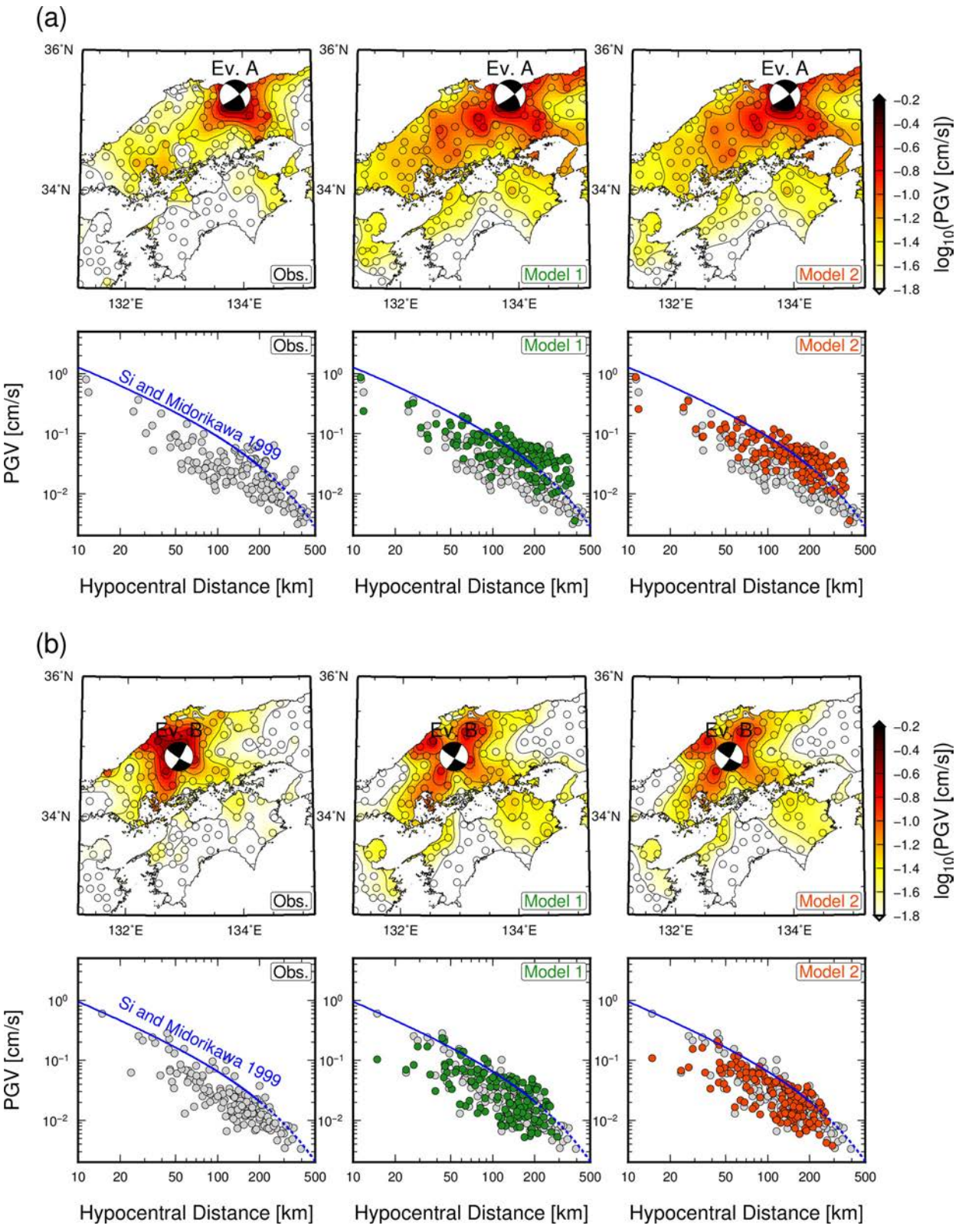

Figure 11. Spatial variation and distance attenuation of peak ground velocities (PGVs) recorded at Hi-net borehole stations during (a) Event A and (b) Event B. Grey, green, and red dots denote observation, simulation of model 1, and simulation of model 2, respectively. Blue solid line is empirical attenuation function of surface PGV proposed by Si & Midorikawa (1999). Blue dashed line is extrapolation of solid line. In order to compensate for the difference between surface and borehole ground motions, empirical attenuation functions are divided by a factor of two.

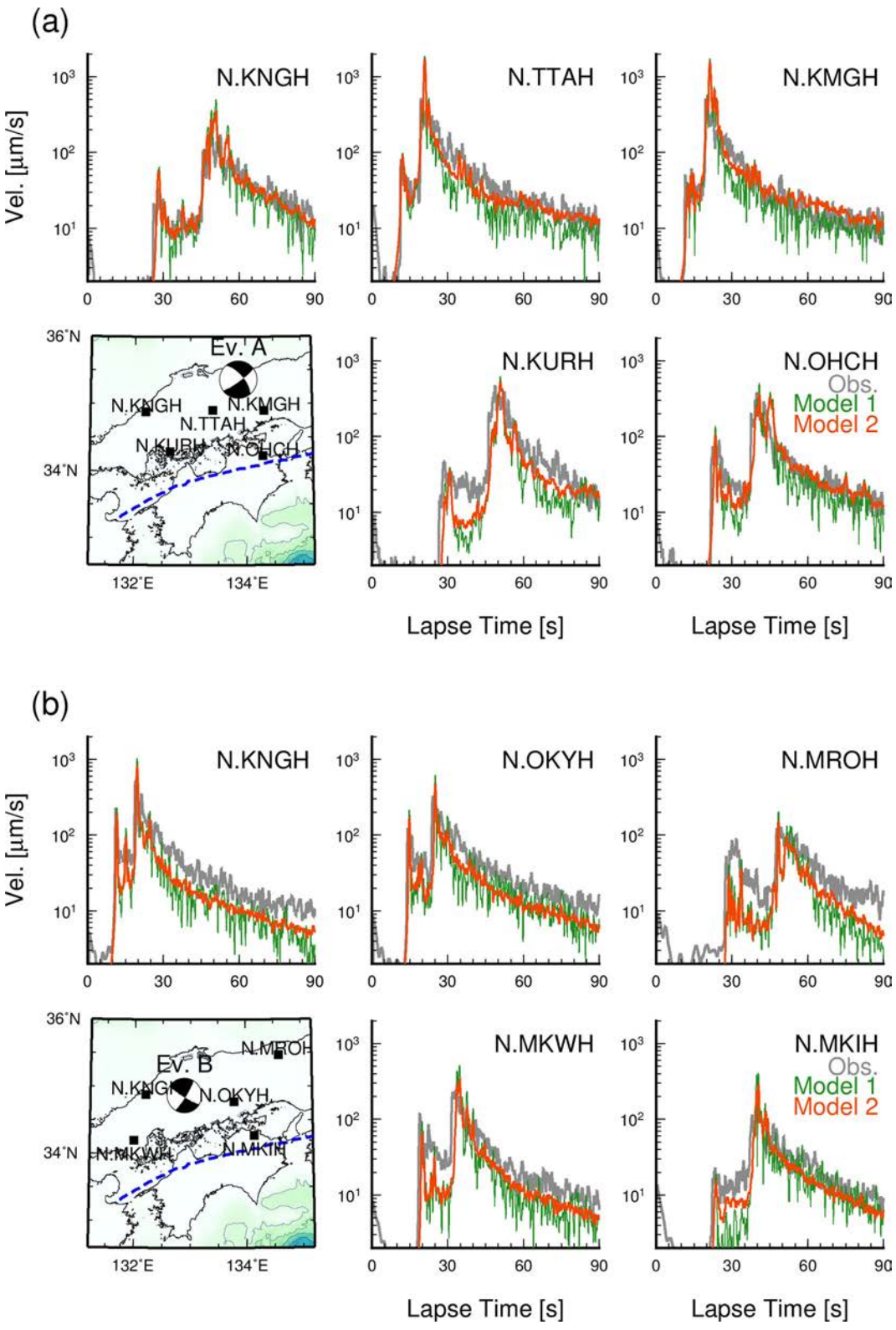

Figure 12. Root mean square (RMS) envelopes for frequencies of 0.1–4 Hz during (a) Event A and (b) Event B. Grey, green, and red lines are observed and simulated envelopes of model 1 and model 2, respectively. Blue dashed line in the map is the MTL of Japan.

5 CONCLUSIONS

We analysed observed and simulated waveforms for modelling high-frequency seismic wave propagation during crustal earthquakes in a heterogeneous crust. Small-scale velocity heterogeneity within the crust, which contributes to distortion of the apparent radiation patterns and scattering attenuation, could be characterized by an exponential-type PSDF with a correlation length of 1 km and an RMS value of 0.03. Intrinsic attenuations of *P* and *S* waves were also estimated by direct comparisons of observed and simulated attenuations of maximum amplitudes. Estimated $Q_{P.\mathrm{int}}{}^{-1}$ and $Q_{S.\mathrm{int}}{}^{-1}$ values range from $10^{-2.6}$ to $10^{-2.0}$ and $10^{-2.8}$ to $10^{-2.4}$, respectively, indicating $Q_{P.\mathrm{int}}{}^{-1} > Q_{S.\mathrm{int}}{}^{-1}$ for high frequencies (>1 Hz). We also found that scattering attenuation due to small-scale velocity heterogeneity has a very small contribution to the observed apparent attenuation, suggesting that intrinsic attenuation is the dominant attenuation mechanism in the crust.

Using the estimated practical parameter set of small-scale velocity heterogeneity and $Q_{S.\mathrm{int}}{}^{-1}$, we conducted FDM simulations of moderate crustal earthquakes. Our simulations successfully reproduced the observed PGVs, characteristics of record sections, and coda envelopes, indicating that the parameters estimated in our study are suitable for physics-based evaluations of seismic ground motions during crustal earthquakes. We believe that our structure model could also be applicable for simulations of larger earthquakes, which can cause strong ground motions and severe damage to man-made structures, using finite-fault models.

In our simulations, a simple point source assumption was employed. Recent studies revealed that rupture directivity effects are also present, even for small-to-moderate earthquakes (e.g. Boatwright 2007; Pacor *et al*. 2016). Furthermore, fault damage zones characterized by velocities 20–30 per cent lower compared to surrounding structures (e.g. Lewis & Ben-Zion 2010) would also affect near-fault strong ground motions (e.g. Graves & Pitarka 2016). Earthquakes used in this study occurred near the faults of the 1943 Tottori (*M* 7.4) and the 2000 Tottori-ken Seibu (M_{w} 6.6) earthquakes, where complex fault systems are developed (Fukuyama *et al*. 2003) and fault damage zones are also expected (Asano & Hasegawa 2004). Other localized strong heterogeneities in the crust were also detected in regions with rich fluid environments (e.g. Takahashi *et al*. 2009; Takemura & Yoshimoto 2014; Takemura *et al*. 2015b), although small-scale velocity heterogeneities are also uniformly distributed within our crust model. In future studies, detailed analysis will be conducted to reveal the effects of rupture and localized heterogeneities on the observed seismic wavefield and to achieve more precise simulations of seismic wave propagation.

ACKNOWLEDGEMENTS

Hi-net and F-net waveform data, the Hi-net hypocentre catalogue and F-net MT solutions are available via the website of the National Research Institute for Earth Science and Disaster Resilience, Japan (http://www.hinet.bosai.go.jp/). The frequency response of the short-period Hi-net sensors with a natural frequency of 1 Hz was corrected using the program of Maeda *et al*. (2011) via their GitHub page (https://github.com/takuto-maeda/hinet_decon/releases). Bathymetric data were obtained from ETOPO1 (Amante & Eakins 2009). Generic Mapping Tools (Wessel & Smith 1998) and Seismic Analysis Code (SAC) were used to create figures and conduct signal processing, respectively. The FDM simulations of seismic wave propagation were conducted on the computer system of the Earthquake and Volcano Information Centre at the Earthquake Research Institute, University of Tokyo, and the Earth Simulator of the Japan Agency for Marine-Earth Science and Technology. This work was supported by a collaborated research program of the Earthquake Research Institute, the University of Tokyo (#2015-B-01). ST is grateful for the fanatical support provided by the Grants-in-Aid for the Japan Society for the Promotion of Science (#17K14382). We also thank Prof U. Wegler, an anonymous reviewer, and the editor Dr A. Ferreira for their careful reading and constructive comments that significantly improved the manuscript.

REFERENCES

Aki, K., 1980. Attenuation of shear waves in the lithosphere for frequencies from 0.05 to 25 Hz, *Phys. Earth planet. Inter.,* **21,** 50–60.

Aki, K. & Richards, P., 2002. *Quantitative Seismology,* 2nd edn, University Science Books.

Amante, C & Eakins, B.W., 2009. ETOPO1 Arc-Minute Global Relief Model: Procedure, data sources and analysis: NOAA Technical Memorandum NESDIS NGDC-24, National Geophysical Data Center, NOAA, doi:10.7289/V5C8276M.

Archuleta, R. & Ji, C., 2016. Moment rate scaling for earthquakes 3.3 $\leq$ M $\leq$ 5.3 with implications for stress drop, *Geophys. Res. Lett.,* **43,** doi:10.1002/2016GL071433.

Asano, Y. & Hasegawa, A., 2004. Imaging the fault zones of the 2000 western Tottori earthquake by a new inversion method to estimate three-dimensional distribution of the scattering coefficient, *J. geophys. Res.,* **109,** B06306, doi:10.1029/2003JB002761.

Baltay, A. & Beroza, G., 2013. Ground motion prediction from tremor, *Geophys. Res. Lett.,* **40,** 1–6.

Birch, A.F., 1961. The velocity of compressional waves in rocks to 10 kilobars, part 2, *J. geophys. Res.,* **66,** 2199–2224.

Boatwright, J., 2007. The persistence of directivity in small earthquakes, *Bull. seism. Soc. Am.,* **97,** 1850–1861.

Boatwright, J., Fletcher, J.B. & Fumal, T.E., 1991. A general inversion scheme for source, site, and propagation characteristics using multiply recorded sets of moderate-sized earthquakes, *Bull. seism. Soc. Am.,* **81,** 1754–1782.

Boore, D.M. & Boatwright, J., 1984. Average body-wave radiation coefficients, *Bull. seism. Soc. Am.,* **74,** 1615–1621.

Boore, D.M. & Joyner, W.B., 1982. The empirical prediction of ground motion, *Bull. seism. Soc. Am.,* **72,** S43–S60.

Bostock, M.G., Thomas, A.M., Savard, G., Chuang, L. & Rubin, A.M., 2015. Magnitudes and moment-duration scaling of low-frequency earthquakes beneath southern Vancouver Island, *J. geophys. Res.,* **120,** 6329–6350.

Carcolé, E. & Sato, H., 2010. Spatial distribution of scattering loss and intrinsic absorption of short-period *S* waves in the lithosphere of Japan on the basis of the Multiple Lapse Time Window Analysis of Hi-net data, *Geophys. J. Int.,* **180,** 268–290.

Efron, B. & Tibshirani, R., 1986. Bootstrap methods for standard errors, confidence intervals, and other measures of statistical accuracy, *Stat. Sci.,* **1**(1), 54–77.

Fehler, M., Hoshiba, M., Sato, H. & Obara, K., 1992. Separation of scattering and intrinsic attenuation for the Kanto-Tokai region, Japan, using measurements of *S*-wave energy versus hypocentral distance, *Geophys. J. Int.,* **108,** 787–800.

Fukuyama, E., Ishida, M., Dreger, D.S. & Kawai, H., 1998. Automated seismic moment tensor determination by using on-line broadband seismic waveforms, *Zisin, J. Seismol. Soc. Japan,* **51,** 149–156 (in Japanese with English abstract).

Fukuyama, E., Ellsworth, W.L., Waldhauser, F. & Kubo, A., 2003. Detailed fault structure of the 2000 western Tottori, Japan, earthquake sequence, *Bull. seism. Soc. Am.,* **93,** 1468–1478.

Furumura, T., 2016. Destructive near-fault strong ground motion from the 2016 Kumamoto prefecture, Japan, M7.3 earthquake, *Landslides,* **13**(6), 1519–1524.

Furumura, T. & Chen, L., 2004. Large scale parallel simulation and visualization of 3D seismic wavefield using the Earth simulator, *Comput. Model. Eng. Sci.,* **6,** 153–168.

Furumura, T., Kennett, B.L.N. & Koketsu, K., 2003. Visualization of 3D wave propagation from the 2000 Tottori-ken, Seibu, Japan, earthquake: observation and numerical simulation, *Bull. seism. Soc. Am.,* **93,** 870–881.

Furumura, T., Hong, T.K. & Kennett, B.L.N., 2014. *Lg* wave propagation in the area around Japan: observations and simulations, *Prog. Earth Planet. Sci.,* **1,** 10, doi:10.1186/2197-4284-1-10.

Gaebler, P.J., Eulenfeld, T. & Wegler, U., 2015. Seismic scattering and absorption parameters in the W-Bohemia/Vogtland region from elastic and acoustic radiative transfer theory, *Geophys. J. Int.,* **203,** 1471–1481.

Graves, R. & Pitarka, A., 2016. Kinematic ground-motion simulations on rough faults including effects of 3D stochastic velocity perturbations, *Bull. seism. Soc. Am.,* **106,** 2136–2153.

Hartzell, S., Meremonte, M., Ramírez-Guzmán, L. & McNamara, D., 2014. Ground motion in the presence of complex topography: earthquake and ambient noise sources, *Bull. seism. Soc. Am.,* **104,** doi:10.1785/0120130088.

Hartzell, S., Ramírez-Guzmán, L., Meremonte, M. & Leeds, A., 2017. Ground motion in the presence of complex topography II: Earthquake sources and 3D simulations, *Bull. seism. Soc. Am.,* **107,** doi:10.1785/0120160159.

Hoshiba, M., 1993. Separation of scattering attenuation and intrinsic absorption in Japan using the multiple lapse time window analysis of full seismogram envelope, *J. geophys. Res.,* **98,** 15 809–15 824.

Imperatori, W. & Mai, P.M., 2013. Broad-band near-field ground motion simulations in 3-dimensional scattering media, *Geophys. J. Int.,* **192,** 725–744.

Imperatori, W. & Mai, P.M., 2015. The role of topography and lateral velocity heterogeneities on near-source scattering and ground-motion variability, *Geophys. J. Int.,* **202,** 2163–2181.

Ji, C., Helmberger, D.V., Wald, D.J. & Ma, K.F., 2003. Slip history and dynamic implications of the 1999 Chi-Chi, Taiwan earthquake, *J. geophys. Res.,* **108,** 2412, doi:10.1029/2002JB001764.

Jin, A., Mayeda, K., Ada, S.D. & Aki, K., 1994. Separation of intrinsic and scattering attenuation in southern California using TERRAscope data, *J. geophys. Res.,* **99**,17 835–17 848.

Kamigaichi, O. *et al.*, 2009. Earthquake Early Warning in Japan: warning the general public and future prospects, *Seimol. Res. Lett.,* **80,** 717–726.

Kanamori, H. & Brodsky, E., 2004. The physics of earthquakes, *Rep. Prog. Phys.,* **67,** 1429–1496.

Kita, S. & Matsubara, M., 2016. Seismic attenuation structure associated with episodic tremor and slip zone beneath Shikoku and the Kii Peninsula, southestern Japan, in the Nankai subduction zone, *J. geophys. Res.,* **121,** 1962–1982.

Klimeš, L., 2002. Correlation functions of random media, *Pure appl. Geophys.,* **159,** 1811–1831.

Kobayashi, M., Takemura, S. & Yoshimoto, K., 2015. Frequency and distance changes in the apparent *P*-wave radiation pattern: effects of seismic wave scattering in the crust inferred from dense seismic observations and numerical simulations, *Geophys. J. Int.,* **202,** 1895–1907.

Koketsu, K., Miyake, H. & Suzuki, H., 2012. Japan integrated velocity structure model version 1, in *Proceedings of the 15th World Conference on Earthquake Engineering,* Lisbon, Portugal, September 24–28.

Kubo, A., Fukuyama, E., Kawai, H. & Nonomura, K., 2002. NIED seismic moment tensor catalogue for regional earthquakes around Japan: quality test and application, *Tectonophysics,* **356,** 23–48.

Kubo, H., Asano, K., Iwata, T. & Aoi, S., 2016. Development of fully Bayesian multiple-time-window source inversion, *Geophys. J. Int.,* **204,** 1601–1619.

Kumagai, H., Saito, T., O'Brien & Yamashina, T., 2011. Characterization of scattered seismic wavefields simulated in heterogeneous media with topography, *J. geophys. Res.,* **116,** B03308, doi:10.1029/2010JB007718.

Lewis, M.A. & Ben-Zion, Y., 2010. Diversity of fault zone damage and trapping structures in the Parkfield section of the San Andreas Fault from comprehensive analysis of near fault seismograms, *Geophys. J. Int.,* **183,** 1579–1595.

Liu, H. & Helmberger, D.V., 1985. The 23:19 aftershock of the 15 October 1979 Imperial Valley earthquake: more evidence for an asperity, *Bull. seism. Soc. Am.,* **75,** 689–708.

Liu, X. & Zhao, D., 2015. Seismic attenuation tomography of the southwest Japan arc: new insight into subduction dynamics, *Geophys. J. Int.,* **201,** 134–156.

Maeda, T., Obara, K., Furumura, T. & Saito, T., 2011. Interference of long-period seismic wavefield observed by the dense Hi-net array in Japan, *J. geophys. Res.,* **116,** B10303, doi:10.1029/2011JB008464.

Maeda, T., Furumura, T., Noguchi, S., Takemura, S., Sakai, S., Shinohara, M., Iwai, K. & Lee, SJ., 2013. Seismic- and tsunami-wave propagation of the 2011 off the Pacific coast of Tohoku earthquake as inferred from the tsunami-coupled finite-difference simulation, *Bull. seism. Soc. Am.,* **103**(2B), 1456–1472.

Margerin, L., Campilo, M., Shapiro, N.M. & Tiggelen, B.V., 1999. Residence time of diffuse waves in the crust as a physical interpretation of coda Q: application to seismograms recorded in Mexico, *Goephys. J. Int.,* **138,** 343–352.

Matsubara, M., Sato, H., Ishiyama, T. & Van Horne, A., 2017. Configuration of the Moho discontinuity beneath the Japan Islands derived from three-dimensional seismic tomography, *Tectonophysics,* **710–711,** 97–107.

Morioka, H., Kumagai, H. & Maeda, T., 2016. Numerical and theoretical investigation of isotropic radiation of *S* waves at volcanoes, in *AGU Fall Meeting 2016,* S53A-2788, San Francisco.

Obara, K., Kasahara, K., Hori, S. & Okada, Y., 2005. A densely distributed high-sensitivity seismograph network in Japan: Hi-net by National Research Institute for Earth Science and Disaster Prevention, *Rev. Sci. Instrum.,* **76,** 021301, doi:10.1063/1.1854197.

Okada, Y., Kasahara, K., Hori, S., Obara, K., Sekiguchi, S., Fujiwara, H. & Yamamoto, A., 2004. Recent progress of seismic observation networks in Japan –Hi-net, F-net, K-NET and KiK-net–, *Earth Planets Space,* **56,** xv–xxviii.

Pacor, F., Gallovič, F., Puglia, R., Luzi, L. & D'Amico, M., 2016. Diminishing high-frequency directivity due to a source effect: empirical evidence from small earthquakes in the Abruzzo region, Italy, *Geophys. Res. Lett.,* **43,** 5000–5008.

Padhy, S., Wegler, U. & Korn, M., 2007. Seismogram envelope inversion using a multiple isotropic scattering model: application to aftershocks of the 2001 Bhuj earthquake, *Bull. seism. Soc. Am.,* **97,** 222–233.

Robertsson, J., Blanch, J.O. & Symes, W.W., 1994. Viscoelastic finite-difference modeling, *Geophysics,* **59,** 1444–1456.

Sato, H., Nakahara, H. & Ohtake, M., 1997. Synthesis of scattered energy density for nonspherical radiation from a point shear-dislocation source based on the radiative transfer theory, *Phys. Earth planet. Inter.,* **104,** 1–13.

Sato, H., Fehler, M. & Maeda, T., 2012. *Seismic Wave Propagation and Scattering in the Heterogeneous Earth Structure,* 2nd ed., Springer-Verlag.

Satoh, T., 2002. Empirical frequency-dependent radiation pattern of the 1998 Miyagiken-Nanbu earthquake in Japan, *Bull. seism. Soc. Am.,* **92**(3), 1032–1039.

Sawazaki, K., Sato, H. & Nishimura, T., 2011. Envelope synthesis of short-period seismograms in 3-D random media for a point shear dislocation

source based on the forward scattering approximation: application to small strike-slip earthquakes in southwestern Japan, *J. geophys. Res.,* **116,** B08305, doi:10.1029/2010JB008182.

Shiomi, K., Obara, K. & Sato, H., 2006. Moho depth variation beneath southwestern Japan revealed from the velocity structure based on receiver function inversion, *Tectonophysics,* **420,** 205–221.

Si, H. & Midorikawa, S., 1999. New attenuation relations for peak ground acceleration and velocity considering effects of fault type and site condition, *J. Struct. Constr. Eng., AIJ,* **523,** 63–70 (in Japanese with English abstract).

Takahashi, T., 2012. Three-dimensional attenuation structure of intrinsic absorption and wide-angle scattering of *S* waves in northeastern Japan, *Geophys. J. Int.,* **189,** 1667–1680.

Takahashi, T., Sato, H., Nishimura, T. & Obara, K., 2009, Tomographic inversion of the peak delay times to reveal random velocity fluctuations in the lithosphere: method and application to northeastern Japan, *Geophys. J. Int.,* **178,** 1437–1455.

Takemura, S. & Yoshimoto, K., 2014. Strong seismic wave scattering in the low-velocity anomaly associated with subduction of oceanic plate, *Geophys. J. Int.,* **197,** 1016–1032.

Takemura, S., Furumura, T. & Saito, T., 2009. Distortion of the apparent *S*-wave radiation pattern in the high-frequency wavefield: Tottori-ken Seibu, Japan, earthquake of 2000, *Geophys. J. Int.,* **178,** 950–961.

Takemura, S., Furumura, T. & Maeda, T., 2015a. Scattering of high-frequency seismic waves caused by irregular surface topography and small-scale velocity inhomogeneity, *Geophys. J. Int.,* **201,** 459–474.

Takemura, S., Yoshimoto, K. & Tonegawa, T., 2015b. Scattering of trapped *P* and *S* waves in the hydrated subducting crust of the Philippine Sea Plate at shallow depths beneath the Kanto region, Japan, *Geophys. J. Int.,* **203,** 2261–2276.

Takemura, S., Akatsu, M., Masuda, K., Kajikawa, K. & Yoshimoto, K., 2015c. Long-period ground motions in a laterally inhomogeneous large sedimentary basin: observations and model simulations of long-period surface waves in the northern Kanto Basin, Japan, *Earth Planets Space,* **67,** 33, doi:10.1186/s40623-015-0201-7.

Takemura, S., Kobayashi, M. & Yoshimoto, K., 2016. Prediction of maximum *P*- and *S*-wave amplitude distributions incorporating frequency- and distance-dependent characteristics of the observed apparent radiation patterns, *Earth Planets Space,* **68,** 166, doi:10.1186/s40623-016-0544-8.

Takenaka, H., Mamada, Y. & Futamure, H., 2003. Near-source effect on radiation pattern of high-frequency *S* waves: strong *SH-SV* mixing observed from aftershocks of the 1997 Northwestern Kagoshima, Japan, earthquakes, *Phys. Earth planet. Int.,* **137,** 31–43.

Terakawa, T. & Matsu'ura, M., 2010. The 3-D tectonic stress fields in and around Japan inverted from centroid moment tensor data of seismic events, *Tectonics,* **29,** TC6008, doi:10.1029/2009TC002626.

Ukawa, M., Ishida, M., Matsumura, S. & Kasahara, K., 1984, Hypocenter determination method of the Kanto-Tokai observational network for microearthquakes, *Res. Notes. Natl. Res. Cent. Disaster Prev.,* **53,** 1–88 (in Japanese with English abstract).

Wessel, P. & Smith, W.H.F., 1998. New, improved version of generic mapping tools released, *EOS, Trans. Am. geophys. Un.,* **79,** 579, doi:10.1029/98EO00426.

Yabe, S. & Ide, S., 2014. Spatial distribution of seismic energy rate of tectonic tremors in subduction zones, *J. geophys. Res,* **119,** 8171–8185.

Yabe, S., Baltay, A., Ide, S. & Beroza, G., 2014. Seismic-wave attenuation determined from tectonic tremor in multiple subduction zones, *Bull. seism. Soc. Am.,* **104,**(4), 2043–2059.

Yoshimoto, K., Sato, H. & Ohtake, M., 1993. Frequency-dependent attenuation of *P* and *S* waves in the Kanto area, Japan, based on the coda-normalization method, *Geophys. J. Int.,* **114,** 165–174.

Yoshimoto, K., Takemura, S. & Kobayashi, M., 2015. Application of scattering theory to *P*-wave amplitude fluctuations in the crust, *Earth Planets Space,* **67,** 199, doi:10.1186/s40623-015-0366-0.

Zhang, L., Chen, G., Wu., Y. & Jiang, H., 2016. Stochastic ground-motion simulations for the 2016 Kumamoto, Japan, earthquake, *Earth Planets Space,* **68,** 184, doi:10.1186/s40623-016-0565-3.

SUPPORTING INFORMATION

Supplementary data are available at *GJI* online.

Figure S1. Detailed distribution of epicentres of earthquakes used in our analysis. Focal mechanisms are referred from Hi-net catalogue. Each symbol is same as Fig. 1. Event number is same in Supporting Information Table S1.

Figure S2. (a) Examples of coda-normalized RMS envelopes and (b) distance change in coda-normalized *P*- and *S*-wave amplitudes for frequencies of 0.5–1 and 2–4 Hz. Example envelopes are recorded at N.YSDH during event 25 (Supporting Information Table S1). Time window for calculating averaged coda amplitude is shown below envelopes by blue lines. $|F_p|$ and $|F_s|$ in (b) are values of *P*- and *S*-wave radiation pattern coefficients in 1-D crustal model evaluated using each source parameter (Aki & Richards 2002, Ch. 4). Solid lines in (b) are master attenuation curves from eq. (3).

Figure S3. Comparison of observed and simulated record sections for frequencies of 0.1–4 Hz during (a) Event A and (b) Event B. Velocity seismograms of transverse component at Hi-net stations are plotted. Each trace is multiplied by its hypocentral distance to enhance amplitudes at far stations.

Table S1. Earthquakes used in our analysis. Origin time (JST), hypocentre, focal mechanism, magnitude and duration of *P* and *S* waves are listed.